Earthq Eng & Eng Vib (2021) 20: 161-177 **DOI**: https://doi.org/10.1007/s11803-021-2012-0

Test on mechanical behavior of SRC L-shaped columns under combined torsion and bending moment

Chen Zongping[1, 2†], Ning Fan[1‡], Chen Jianjia[1§], Liu Xiang[1*] and Xu Dingyi[1*]

1. *College of Civil Engineering and Architecture, Guangxi University, Nanning 530004, China*

2. *Key Laboratory of Disaster Prevention and Structure Safety of Chinese Ministry of Education, Nanning 530004, China*

Abstract: Investigations of the seismic behavior of steel reinforced concrete L-shaped columns under constant axial compression and cycled bending-shear-torsion load were performed. Six specimens, which considered two parameters, i.e., the moment ratio of torsion to bending (γ) and the aspect ratio (column length-to-depth ratio, φ), were prepared for the experiment. In this study, the failure process, torsion-displacement hysteresis curves, and flexure-displacement hysteresis curves were obtained. The failure characteristics, mechanical behavior of specimens such as the failure patterns, hysteresis curves, rigidity degradation, ductility and energy dissipation, are analyzed. The experimental research indicated that the major failures of the specimens were bending failure, bending-shear failure and bending-torsion failure as the moment ratio of torsion to bending (γ) increased. The torsion-displacement hysteresis curves were pinched in the middle, formed a slip platform, and the phenomenon of "load drop" occurred after the peak load. The bending-displacement hysteresis curves were plump, which showed that bending capacity of the specimen was better than its torsion capacity. Additionally, the energy dissipation of the specimen was dominated by torsion in the early stage and ultimately governed by the bending moment in the later phase. Test results also indicated that the displacement ductility coefficient and interstory rotation angle of the failure point were less than 3.0 and 1/50, respectively, which means the test specimen performance does not meet the requirement of the Chinese Code for Seismic Design of Buildings (GB 50011-2014) in this respect.

Keywords: compression-bending-shear-torsion combined action; steel reinforced concrete (SRC); L-shaped columns; seismic behavior

1 Introduction

With the development of the economy and society, more and more people have novel ideas about the architecture. Traditional architectural design patterns can no longer satisfy people's requirement for use. Special-shaped columns, such as the L-shaped column, T-shaped column, cross-shaped column and so on, provide an alternative to traditional section columns. Special-shaped sections for different positions, and steel reinforced for higher capacity, which offers the potential advantages of reduced section depth, reduced congestion at the wall boundary region, improved degree of coupling for a given wall width and deformation capacity. It is favored deeply by property owners and dwellers (Ramamurthy and Khan, 1986; Zuo *et al*., 2012; Zhou *et al*., 2012) because the width of the column is the same as the connecting adjacent collinear wall which is conducive to flexibility in the use of architectural space and making the residence comfortable.

Currently, special-shaped columns can be divided into several categories in terms of the combination of materials used, including Steel(S) special-shaped column (Zhang *et al*., 2010; Patton *et al*., 2012), Reinforced Concrete (RC) special-shaped column (Marin, 1979; Li and Pham, 2014; Rong *et al*., 2017), Concrete-filled Steel Tube (CFST) special-shaped column (Shen *et al*., 2013; Patton *et al*., 2014), Steel Reinforced Concrete (SRC) special-shaped column (Liu *et al*., 2019, 2018; Rong *et al*., 2018; Xiao *et al*., 2017; Xue *et al*, 2012, 2017; Chen *et al*., 2016) and so on. However, the S special-shaped column is deficient in terms of fireproofing and corrosion resistance (Sun *et al*., 2015). The RC special-shaped column does not have obvious advantages in bearing capacity, seismic resistance, and application in high-rise buildings due to the inherent defects of its material properties (Yang *et al*., 2010). The CFST special-shaped column has a 90-degree internal corner, which greatly weakens composite actions between steel

Correspondence to: Chen Zongping, College of Civil Engineering and Architecture, Guangxi University, Nanning 530004, China
Tel: +86-13878806048
E-mail: zpchen@gxu.edu.cn
†Professor; ‡PhD Student; §Postgraduate; *PhD

Supported by: National Natural Science Foundation of China under Grant Nos. 51268004 and 51578163, Natural Science Foundation of Guangxi under Grant No 2016GXNSFDA380032 and Bagui Scholar Program of Guangxi under Grant No: [2019]79
Received May 27, 2019; **Accepted** March 19, 2020

and concrete and influences the further function of structural column's bearing capacity (Liang *et al*., 2008). Therefore, when compared with the other three special-shaped columns, the SRC special-shaped column has shown strong functional and economic superiority (Liu *et al*., 2016; Fang *et al*., 2015).

The rapid development of the national economy and infrastructure projects in major cities makes large span, heavy capacity and high-rise buildings more and more common. However, this type of development will inevitably lead to the increase of building self-weight and the emergence of complex stress conditions. Its serious consequences are unpredictable when buildings are subjected to strong earthquakes. Hence, some scholars have carried out basic research on SRC special-shaped columns that are the main load-bearing member of a frame structure. Based on experimental research of fourteen SRC L-shaped short columns and two RC L-shaped short columns under low cyclic reversed loading, Li *et al*. (2008) calculated that the hysteretic loops of the SRC L-shaped short columns were plump and the hysteretic behaviors were improved. Chen *et al*. (2015) finished a series of experimental investigations on seventeen SRC special-shaped columns under low cyclic reversed loading. The test results demonstrated that most displacement ductility coefficients of the specimens were over 3.0, indicating adequate performance in terms of ductility. Furthermore, Xiang *et al*. (2017) researched the design of a SRC T-shaped column-reinforce (RC) concrete beam joint and investigated its seismic behaviors through an experimental study. They found that the SRC T-shaped column-RC beam joint performed well under seismic conditions. Additionally, Chen and Liu (2018) investigated the seismic behavior of nine steel reinforced concrete cross-shaped columns, and found that they exhibited good ductility and deformation capacity.

The horizontal acceleration of seismic waves, as a wave of random probability, has two-dimensional bi-directionality. Under a destructive earthquake, seismic damage indicates that many structures are affected by the additional twist of the column, which will cause the extra loss and damage of the structure (Koliopulos *et al*., 1995). However, the neglecting of the effect of torsion on structural design reduces the safety of the structure (Arnold, 1980; Duan and Chandler, 2010). In this circumstance, different from rectangular columns, the eccentricity between the centroid and shear center of special-shaped columns often produces additional torque under the action of a horizontal earthquake. Therefore, the failure mechanism of SRC special-shaped columns under compression, flexure, shearing, and torsion action should be given the appropriate attention.

However, there have not been many studies about the seismic performance of SRC special-shaped columns under combined torsion except for some experimental results of other types of members. These results showed that the moment ratio of torsion to bending (γ) has significant effects. Otsuka *et al*. (2005) conducted a cyclic loading test on twenty-five specimens subjected to torsional moment, bending moment and axial force. They found that the torsional hysteresis was significantly affected by the moment ratio of torsion to bending (γ). Nie *et al*. (2012, 2013) studied the seismic performance of concrete-filled circular / rectangular steel tube columns under combined torsion. They found that both the torsional and flexural capacities decreased due to combined torsion; specifically, the ultimate lateral load and displacement capacity of the columns decreased as the γ ratio increased. Similarly, due to flexure, the decrease of the γ ratio resulted in the degradation of the torsional moment and lower ultimate twist capacity. Other researchers, such as Hsu *et al*. (2000, 2004) with thirty H-steel sections columns, and Tirasit and Kawashima (2007) with seven RC columns, also found the same interaction effect between torsion and flexure. Li and Belarbi (2012, 2013) conducted the research with three circular RC bridge columns and four square RC bridge columns. They pointed out that the location and length of the damage zone moved upward from the base of the column as the γ ratio increased, with the failure mode and deformation characteristics changed. In addition, Prakash *et al*. (2010) tested eight RC columns under different loading conditions (two were under pure torsion, two were under pure flexure, and four were under combined torsion). Their results showed a significant change in the failure mode and deformation characteristics not only due to the γ ratio but also with the aspect ratio and spiral reinforcement ratio. The test results for twelve circular RC bridge columns under pure bending, pure torsion, and combined loading made by Wang *et al*. (2014) showed that the torsional strength and ductility levels of the column under pure torsion were different in the positive and negative loading cycles, which were caused by the locking and unlocking effect of the spirals. Furthermore, the decreased stirrup spacing contributed additional strength in the positive torsion but provided little benefit in the bending. Greene and Belarbi (2009) developed a model to predict the load-deformation response of a RC member subjected to torsion combined with bending and shear. The twist-rotation behavior, reinforcement stress, and concrete surface strain predicted by the models were in an agreement with the experimental results. Weng *et al*. (2017) carried out quasi-static tests of eleven steel reinforced concrete members under combined torsion. The whole loading process and the failure modes of the specimens were cleared, and the seismic performance indexes of the specimens were analyzed. Wang *et al*. (2018) studied the mechanical behavior of steel tube confined reinforced concrete (STRC) columns under combined compression-bending-torsion, and an experimental investigation was conducted. They found steel tubes can enhance the bending and torsion capacities of reinforced concrete columns, and the reduction of the bending capacity of STRC columns caused by torque were analyzed. Arabzadeh *et al*.

(2018) investigated two aspects of building structures with C-shaped RC walls. The numerical model of the wall was validated against available experimental data. In addition, the dual plastic hinge design method can lower shear force demand along the height of the structure, especially when high torsional flexibility was expected. Chen *et al*. (2018) investigated the mechanical behavior of seven steel reinforced concrete (SRC) columns under combined bending-torsion cyclic loads. The main parameters were torsion moment to bending moment ratios and axial load levels. Finally, they proposed an equation to express the interaction curve between the bending and torsion. Teixeira and Bernardo (2018) studied the torsional ductility of reinforced concrete (RC) beams with rectangular cross section. The following variables study were considered: compressive concrete strength, torsional reinforcement ratio and cross section type (plain or hollow), and important findings were pointed out which could benefit the design of RC beams under torsion. Kaushik and Dasgupta (2019) investigated the behavior of wall-slab junctions and address the shortcomings of the current design requirements subject to strong earthquake shaking. Yuan *et al*. (2018) investigated the torsion-bending ratio effect on seven SRC columns stress and deformation under combined bending and torsion action, and established its calculation methods. Jurkowska (2018) substantiated the necessity of considering the torsional stiffness of reinforced concrete elements in design practice to provide engineers with specialized design techniques, they have been developed for the calculation of torsional stiffness of reinforced concrete elements with normal cracks of rectangular, triangular, T-sections, box-sections, and other cross-sections. Ji *et al*. (2017) used a displacement-based method to improve designs for developed special boundary elements of T-shaped walls. Until very recently, no regulations existed concerning the reasonable design method of special-shaped columns under combined load and torsion. Previous literature shows that there are no studies on the seismic behavior of SRC L-shaped columns under combined loading of compression, flexure, shear, and torsion. In addition, the literature about the interaction between flexural and torsional loads in the behavior of the SRC L-shaped columns is also limited. Therefore, the research program was planned to fill these gaps in the existing literature on the subject and to provide data which could help expand and remove the fundamental barriers to the use of SRC L-shaped columns in the construction industry. In this study, six SRC L-shaped columns with different moment ratios of torsion to bending (γ) and the aspect ratio (φ) were tested by applying constant axial compression and cycled flexure-shear-torsion load to create cyclic composite load and compression fields across the tested region. In addition, the effects of the combined torsion and bending moment on hysteretic torsional and flexural response, failure modes, carrying capacity, ductility characteristics, strength and stiffness degradation, energy dissipation, and interlayer displacement angle will be discussed.

2 Experimental programs

2.1 Specimens details

Six specimens, from ground floor special-shaped columns of a multi-layer frame structure, with different aspect ratios (column length-to-depth ratio (φ)) (i.e., 2.5, 3.0), were designed and fabricated to be representative of typical SRC L-shaped columns as shown in Fig. 1. The model scale is 1/2. According to the difference of φ, the height of the column limb was 360 mm and 300 mm, respectively, and the same section depth was 120 mm. The total height of the column was 1630 mm with an effective height of 1180 mm measured from the bottom of the column to the centerline of the loading points. The moment ratio of shear to span was 3.5 with the cover concrete of 15 mm. The SRC roof plate and base plate were connected to the top and the bottom of the column, with the dimension of 1400 mm × 500 mm × 300 mm and 900 mm × 500 mm × 300 mm, respectively. Eight 12 mm-diameter steel bars were used as longitudinal reinforcements and ten 6 mm-diameter steel bars were used as stirrups. All specimens were tested under combined loading with the moment ratio of torsion to bending (γ) was 0.00, 0.10, 0.18, 0.25, and 0.29 respectively, and the constant axial compression ratio (n) was 0.15. The specimen with γ= 0 was subjected to pure bending.

The characteristic parameters of each specimen are presented in Table 1, where ρ_{ss} represents the steel content in cross section, ρ_s represents the reinforcement ratio, ρ_{sv} represents the volume stirrup rate, and n represents the constant axial compression ratio, $n=N/(Af_c)$, where N is actual axial pressure, f_c is compressive strength of concrete, and A is the full section area.

2.2 Material properties

All specimens were made of ordinary concrete, and three 150 mm × 150 mm × 150 mm cubes were cast and cured with column specimens in the same outdoor conditions. The tested concrete strength was f_{cu} = 39.3 MPa.

Table 2 gives the properties of section steel and steel bars, with f_y, f_u, E_s and ε_y representing the yield strength, ultimate tensile strength, elastic modulus of the steel, and the strains corresponding to yield strength, respectively. The steel specimens used in the material characteristic test were cut from the section steel and steel bars.

All the material characteristic tests were conducted according to the Chinese codes in the *Metallic Materials-Tensile testing-Part 1 Method of test at room temperature* (GB/T 228.1-2010) and *Standard for test method of mechanical properties on ordinary concrete* (GB/T 50081-2002).

2.3 Test setup and procedure

The test setup offered a combined compression, bending, shear, and torsion force with two electro-hydraulic servo actuators, and is shown in Fig. 2. The specimen was mounted vertically on the strong floor, fixed by four steel reaction screws and two girders. Axial load was applied at the top of the column with an axial loading arrangement, which consisted of a hydraulic jack, spherical hinge, roller, loading beam and reaction frame. The combined bending and torsion force was generated by controlling forces and displacements with each actuator followed by the designed loading process. According to different γ ratios of the specimens, different force and displacement were applied by the two actuators, and the horizontal displacements of the specimens were measured by displacement sensors installed in electro-hydraulic servo actuators.

An actual test applied a 100 kN axial load, which began after the loading equipment was checked and the corresponding readings of all instruments were monitored. If everything was in order, the targeted constant axial load was applied and maintained during the test, whereas the lateral forces were cycled. The loading process includes a load-controlled phase and displacement-controlled phase, which is illustrated in Fig. 3. During the load-controlled stage, the load

Table 1 Characteristics of specimen

Specimen No.	γ	φ	ρ_{ss} (%)	ρ_s (%)	ρ_{sv} (%)	n
SRCL-1	0.00	3	7.88	1.26	0.63	0.15
SRCL-2	0.18	3	7.88	1.26	0.63	0.15
SRCL-3	0.10	3	7.88	1.26	0.63	0.15
SRCL-4	0.25	3	7.88	1.26	0.63	0.15
SRCL-5	0.29	3	7.88	1.26	0.63	0.15
SRCL-6	0.25	2.5	8.81	1.57	0.67	0.15

Table 2 Steel material properties

Steel No.	Steel size (mm)	f_y (MPa)	f_u (MPa)	E_s (10^5 MPa)	ε_y (10^{-3})
1	1230×166×5	306.54	430.08	1.85	1.66
2	1230×40×12	311.75	450.76	1.83	1.70
3	1230×70×12	311.75	450.76	1.83	1.70
4	1230×177×5	306.54	430.08	1.85	1.66
5	1230×107×5	306.54	430.08	1.85	1.66
6	1230×117×5	306.54	430.08	1.85	1.66
7	12 (Diameter longitudinal)	498.42	667.08	2.02	2.47
8	6 (Spirals 6@150)	443.21	611.34	1.99	2.23

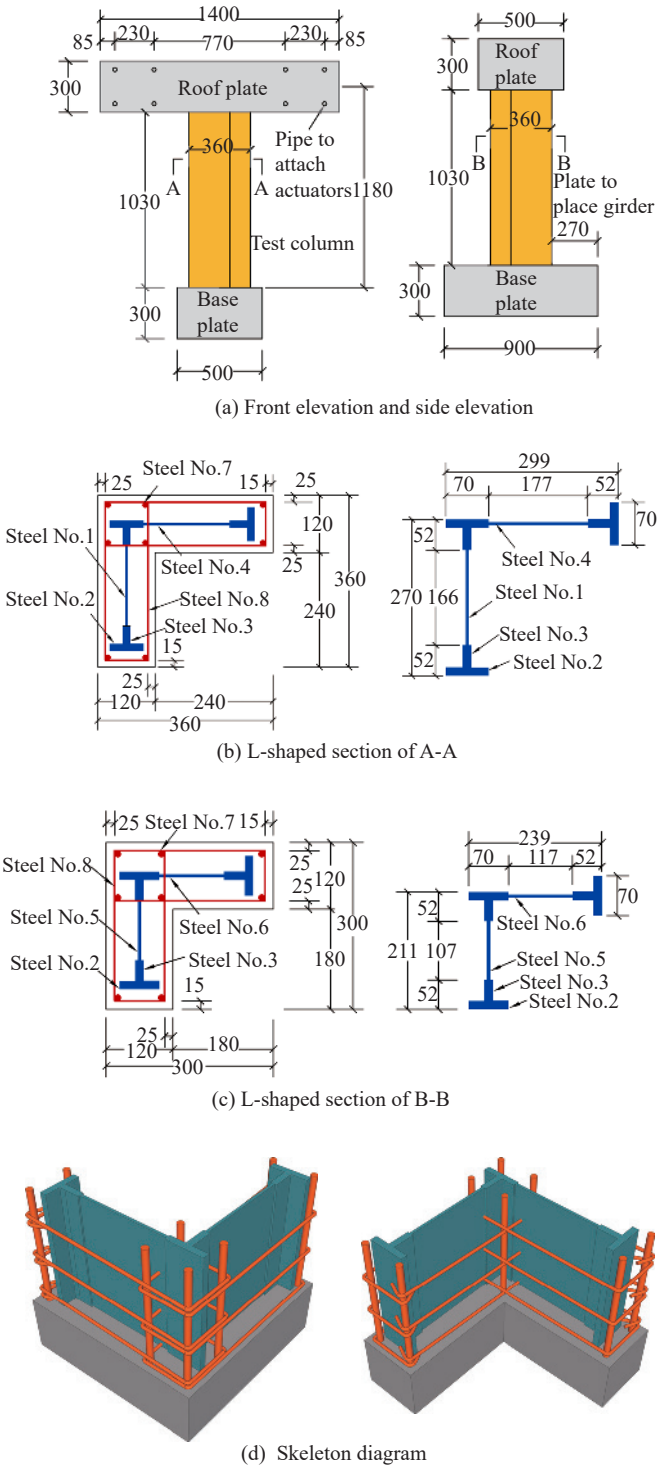

(a) Front elevation and side elevation

(b) L-shaped section of A-A

(c) L-shaped section of B-B

(d) Skeleton diagram

Fig. 1 Detailed design of specimens (Unit: mm)

amplitude is conducted in a single cycle. When the specimen first yielded, the loading process entered the displacement-controlled phase. The horizontal displacement corresponding to the first yield point is named yield displacement Δ_y, which is taken as the standard cyclic displacement for loading amplitude ($n\Delta_y$, n is the integer). In the displacement-controlled phase, the displacement amplitude is conducted in three cycles to measure the indication of strength and

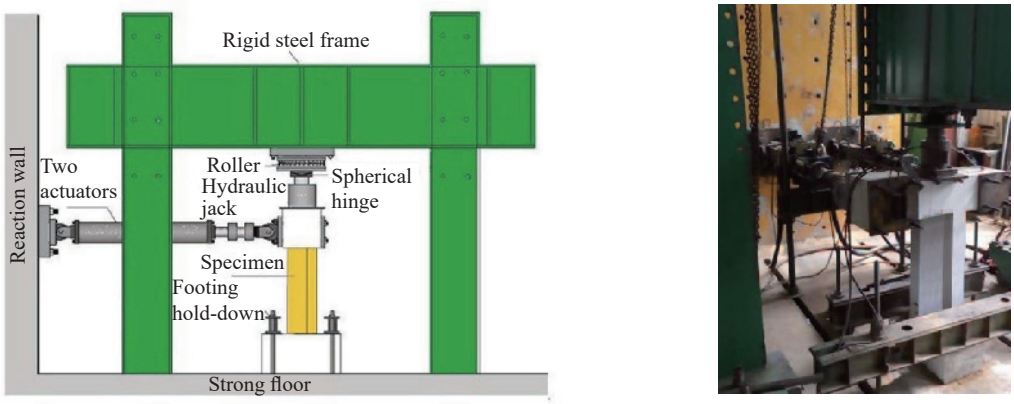

Fig. 2 Test setup

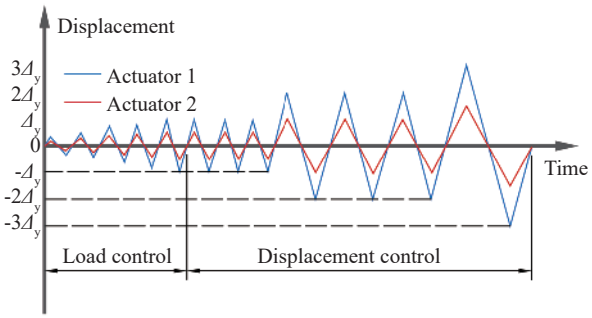

Fig. 3 Loading process

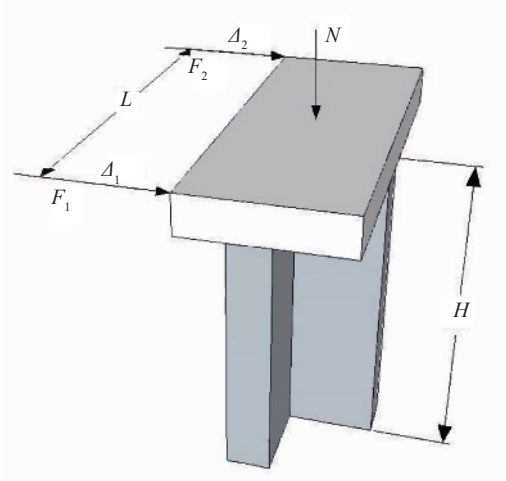

Fig. 4 Loading principle

stiffness degradation characteristics. The test finished when the lateral load resistance deteriorated to 85% of the maximum measured lateral loads.

2.4 Loading principle

Figure 4 shows the loading principle of the test. Two actuators at the top are defined as a primary actuator and secondary actuator, respectively. The force applied by the primary actuator was named F_1, and accordingly, the force applied by the secondary actuator was named F_2. The force system, consisting of F_1 and F_2, was converted by equivalent transformation, acting on the bottom cross section of the column. The torsion T and flexure M can be calculated by Eqs. (1)–(2):

$$T = F_1 L_1 - F_2 L_2 \tag{1}$$

$$M = (F_1 + F_2) H \tag{2}$$

According to Eqs. (1)–(2), the moment ratio of torsion to bending γ and the moment ratio of shear to span λ can be calculated by Eqs. (3)–(4)

$$\gamma = \frac{T}{M} = \frac{(F_1 L_1 - F_2 L_2)}{(F_1 + F_2) H} \tag{3}$$

$$\lambda = \frac{M}{V h_0} = \frac{H}{h_0} \tag{4}$$

The horizontal displacement Δ and the twist angle θ at the top of the column can be calculated by Eqs. (5)-(6)

$$\Delta = 0.548\Delta_1 + 0.452\Delta_2 \tag{5}$$

$$\theta = \frac{(\Delta_2 - \Delta_1) \times 360}{(\pi L)} \tag{6}$$

where h_0 represents the height of L-shaped section, and V represents the shear acting on the bottom cross section of the column. L is the distance of the loading action point. L_1, Δ_1 represent the distance of the F_1 action point to the section centroid and the horizontal displacement of the F_1 action point, respectively. L_2, Δ_2 represent the distance of the F_2 action point to the section centroid and the horizontal displacement of the F_2 action point, respectively, and H represents the tested length from the lateral loading point to the top of the base plate.

3 Failure modes

Along with the increase of γ, the failure pattern translates from bending failure (γ = 0) to bending-shear failure (γ = 0.10 to 0.18) and bending-torsion failure (γ= 0.25 to 0.29). The cracks and failure patterns of the specimens are shown in Figs. 5–7.

3.1 Bending failure

The specimens with γ=0 were damaged by bending. The main damage characteristics are as follows. At the beginning of the loading test, the first main horizontal flexural fracture occurred in the middle and lower part of the column at the A surface and C surface, vertical to

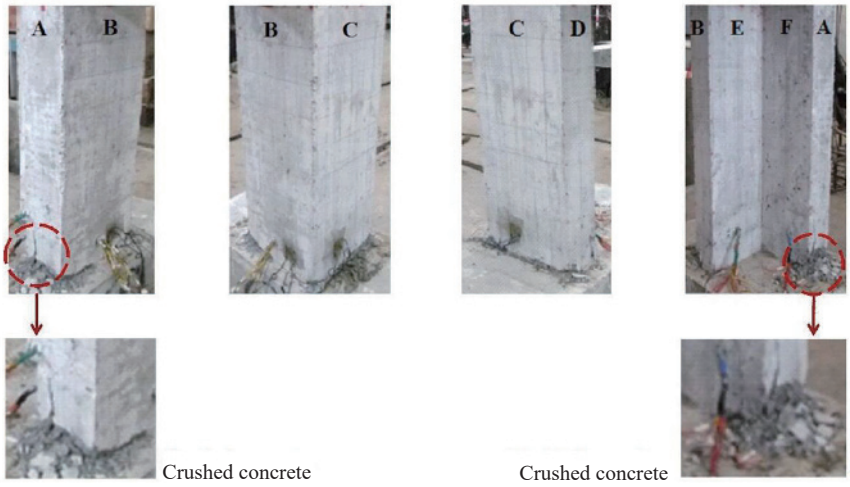

Fig. 5 Failure mode of specimen with γ = 0

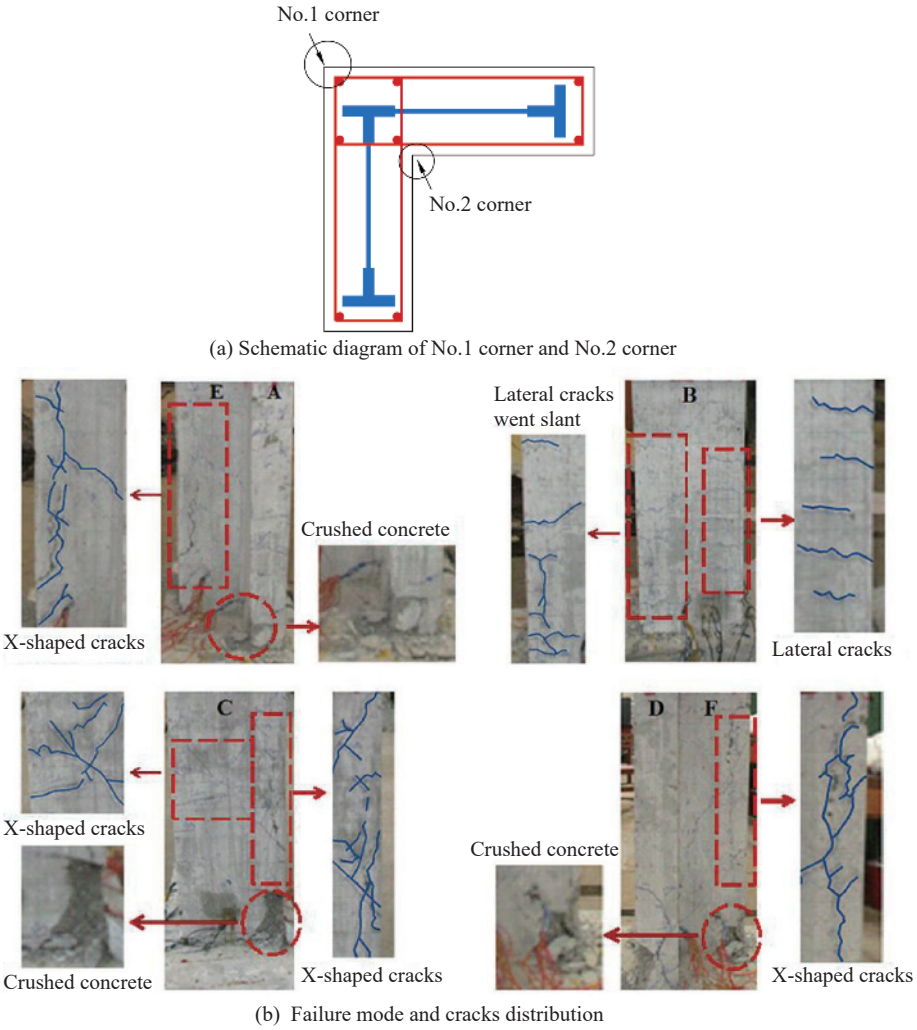

(a) Schematic diagram of No.1 corner and No.2 corner

(b) Failure mode and cracks distribution

Fig. 6 Failure mode of specimen with γ = 0.10 to 0.18

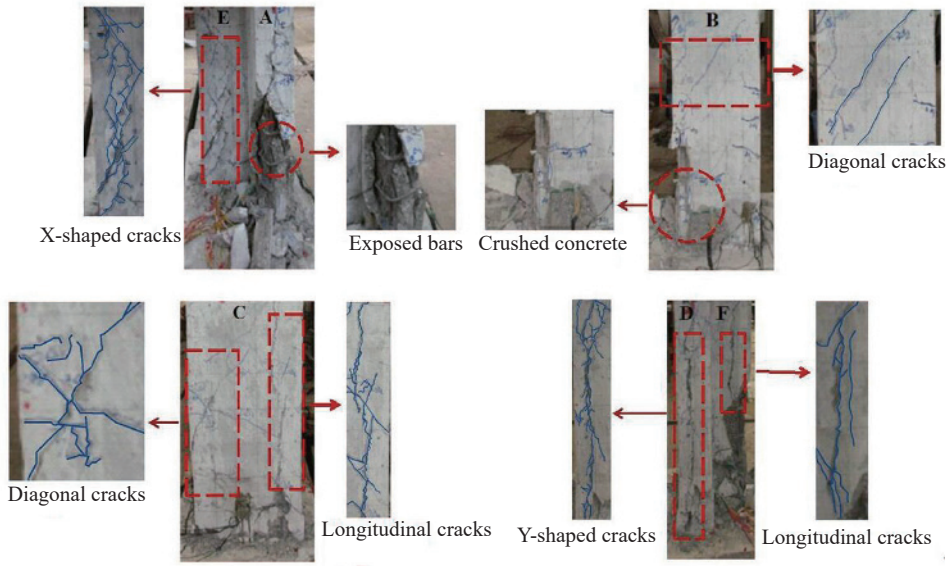

Fig. 7 Failure mode of specimen with γ = 0.25 to 0.29

the loading direction. With the increase of the load, the original fracture extended and widened, and there was an increasing number of lateral cracks along the fracture sides. Meanwhile, at the B surface and F surface, new horizontal cracks appeared on the edge and slant cracks appeared in the middle. At the end of loading, the concrete was compressed and fell out at the A surface, vertical to the loading direction. Steel bars were exposed; moreover, a horizontal fracture zone appeared at the bottom of the C surface, and the distribution resembled a narrow-band. The test concluded.

3.2 Bending-shear failure

The specimens with γ=0.10 to 0.18 were damaged by bending shear. The main damage characteristics are as follows. At the beginning of the loading test, at the B surface, at the mid-height and below, cracks occurred laterally and then they became slanted. With the increase of the load, an increasing number of lateral cracks occurred and these cracks became slated at the No.1 corner. On the side C, cracks initiated at two edges and propagated at a slant into the center then the distribution looked like an X-shape. At the same time, there were many obvious fractures at the corner No. 2, which formed an X-shape, and then the distribution gradually looked like a reticulation. At the end of the load loading test, the volume of concrete expanded and the concrete at the core of the X-shaped crack group fell out. Meanwhile, at the A surface, B surface, and F surface, the concrete was compressed and fell out, and steel bars were exposed. Moreover, the failure area of this specimen was larger than the one which was damaged by bending. The test concluded. At the end, lateral cracks perpendicular to the push direction occurred in the part of the column at mid-height and below, which showed that the bending moment had a significant effect on this type of specimen. The appearance of diagonal cracks and the concrete were compressed and fell out near the base plate, which showed the obvious influence of shear force.

3.3 Bending-torsion failure

The specimens with γ=0.25 to 0.29 were damaged by bending torsion. The main damage characteristics are as follows. At the beginning of the loading test, several cracks appeared concurrently and then became slanted in the mid-height of the A surface. With the increase of the load, the torsion moment had a significant effect on the appearance of the diagonal cracks. The growing number of diagonal cracks occurred on the entire surface of the specimen and these cracks crisscrossed. Remarkably, some of the cracks formed an X-shape, and some of them connected to several longitudinal cracks and then formed a Y-shape or inverted Y-shape at the No. 2 corner. The volume of concrete expanded and the concrete at the core of the X-shaped crack group or the Y-shaped crack group fell out. Finally, the longitudinal cracks became extended and widened at the A surface, followed by concrete crush, and section steel and steel bars were exposed. The test concluded.

4 Test results analysis

4.1 Hysteretic curve

Figures 8 and 9 show the torsion moment versus rotation angle hysteretic curves and the bending force versus displacement hysteretic curves of the specimens, respectively, where T represents the torsion moment, θ represents the rotation angle, M represents the bending

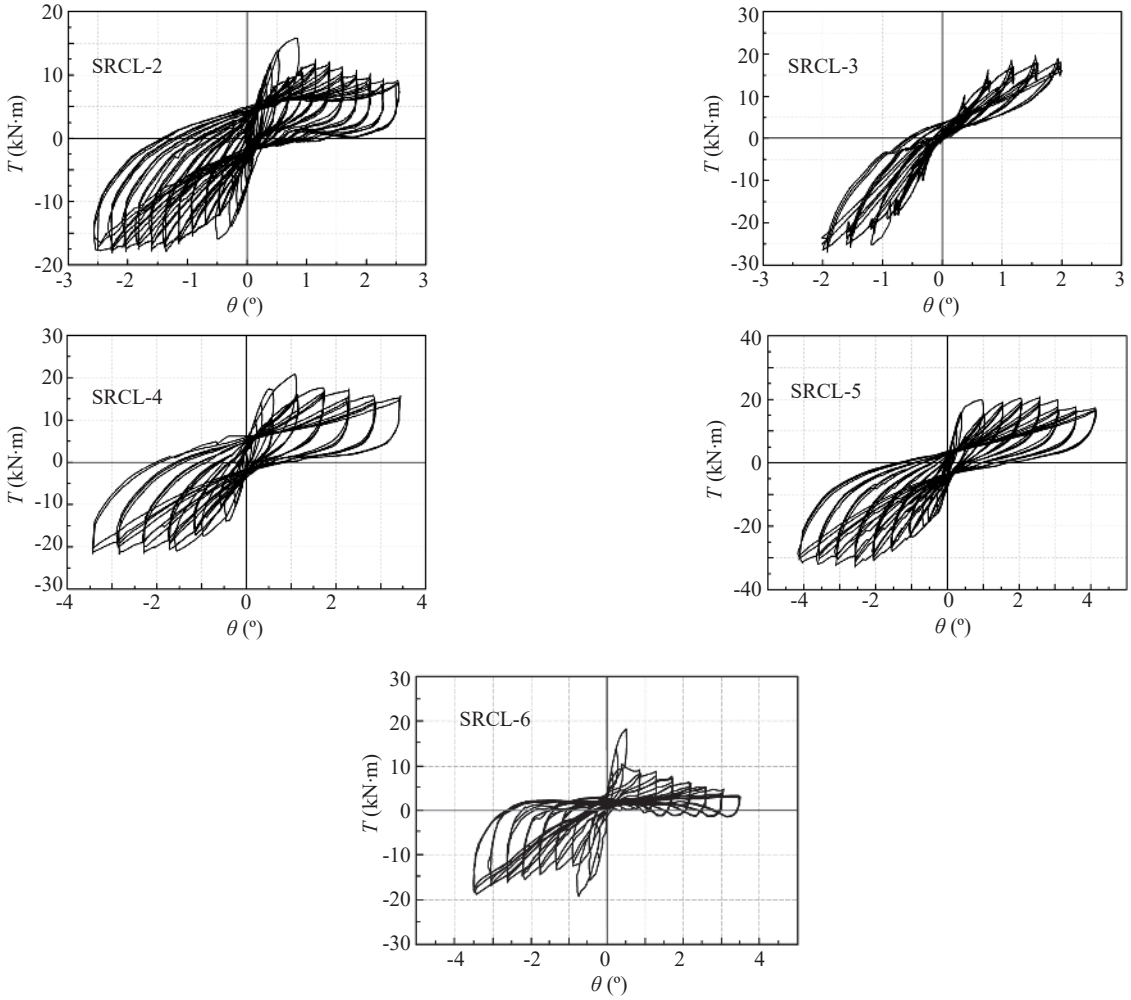

Fig. 8 Torsion-rotation angle hysteretic loops (γ decreases from left to right)

moment, and Δ represents the horizontal displacement. Three conclusions from Figs. 8 and 9 are as follows.

(1) The bending force versus displacement hysteretic curves of the specimens basically formed an S-shape or anti-S-shape, and pinching is obvious, indicating that the influence of bond slip could not be ignored. The torsion moment versus rotation angle hysteretic curves are the same.

(2) The hysteretic curves of the torsion moment versus rotation angle are asymmetric, and the variation tendency of the bending force versus displacement hysteretic curves is the same. The area of the rotation angle hysteresis loop in the positive direction is smaller than that in the negative direction, and if the specimen has a large φ, it will be larger than the small one. Meanwhile, another of the two-type curves is reversed. This is mainly because the W_p (section modulus in torsion) and W_z (section modulus in bending) of the L-shaped section is asymmetrical in two directions.

(3) After the peak point of torsion load, there is an obvious "load drop" phenomenon in the torsion moment versus rotation angle hysteretic curve, and the stiffness and strength of the specimen decreased rapidly. The main reason is that the concrete around the steel skeleton cracked and fell off because the bond slip cracks extended and widened and became worse, the combined action of pressure and tension led to a sharp decrease in the torsional stiffness. As seen from Fig. 8, a smaller γ makes this phenomenon more obvious. Furthermore, the phenomenon eases with the increase of γ. This also indicates that the bending moment governs the loading and failure process of the specimen after the plastic stage, which means the specimens were eventually destroyed by the bending force.

Compared with the moment displacement hysteretic curve of the steel reinforced concrete rectangular column, the moment displacement hysteretic curve of the rectangular column is plumper. Similarity, the slip platform is obviously in the torsion-rotation angle hysteretic curves of the middle pinch. It is shown that the bending capacity of the L-shaped columns is slightly inferior to that of the rectangular columns; however, there is little difference in torsion capacity. The bending capacity of the two types of columns is better than the torsion capacity.

The measured bending-torsion M-T interaction curves are shown Fig. 10. The figure shows the bending moment and torsion moment corresponding to the

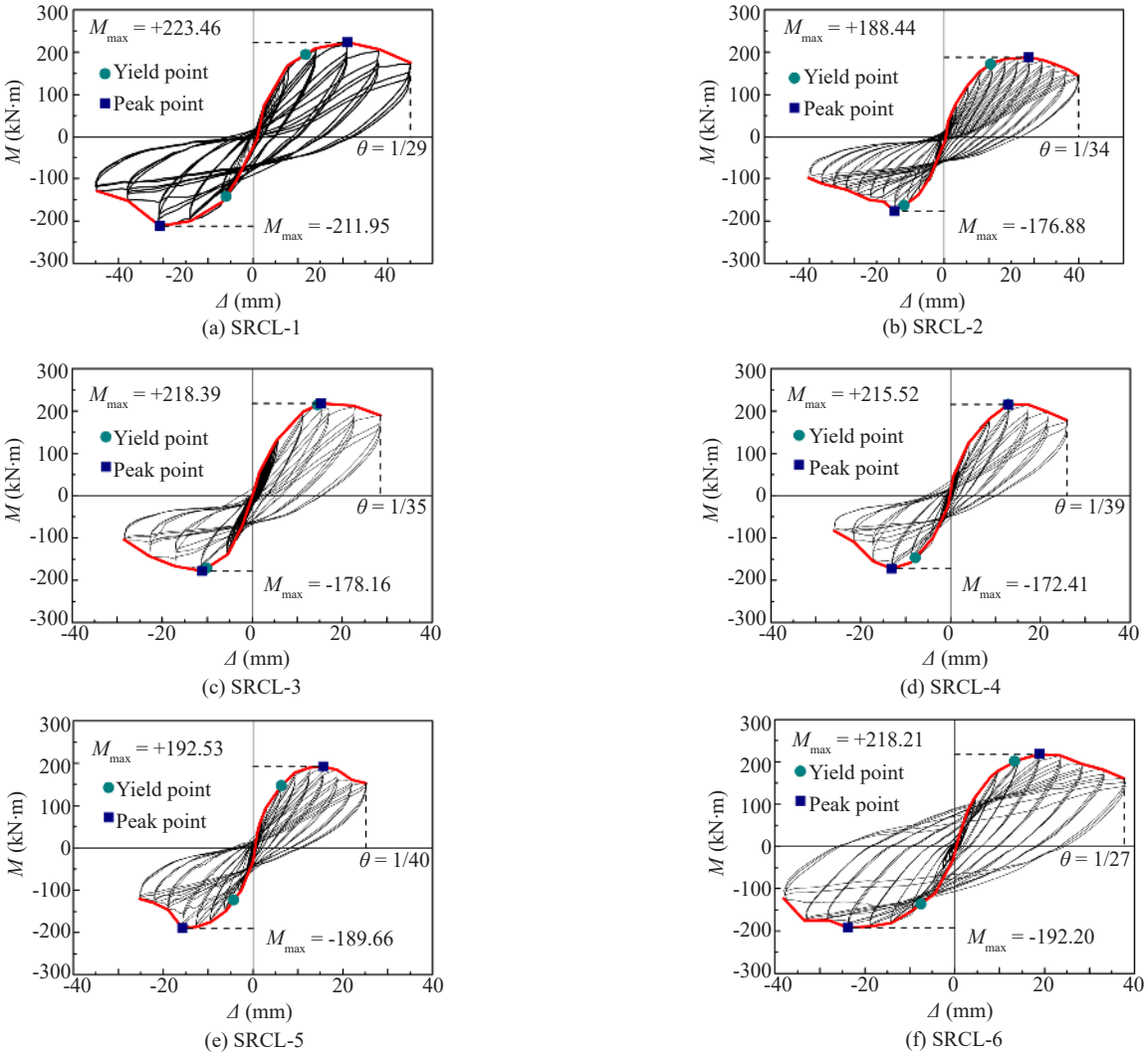

Fig. 9 Bending-displacement hysteretic loops (γ decreases from left to right)

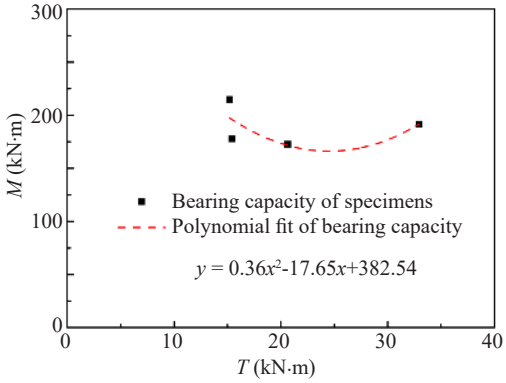

Fig. 10 Measured bending-torsion *M-T* interaction curve

maximum bearing capacity of the specimens in the push direction. It does not contain data from the SRCL-6 specimen because its data is not complete. It can be seen from Fig.10 that the bearing capacity of the specimen will rise slightly after falling with the aspect ratio of 3.0 and the motion ratio of torsion to bending (γ) is 0.10 to 0.29.

It can be concluded that sufficient residual bearing capacity should be reserved in consideration of the bearing capacity of the construction member in the actual design. For the members designed to have better torsion capacity, the structural measures of strengthening torsion resistance should actively be taken, such as controlling the volume stirrup ratio, using the stirrup form of composite stirrup or reinforced spiral stirrup, adding studs and so on.

4.2 Backbone curve

Figure 11 gives the torsion moment versus rotation angle backbone curves and the bending force versus displacement hysteretic backbone curves. As shown in the figure:

(1) The skeleton lines of the torsion moment versus rotation angle backbone curves and the bending force versus displacement hysteretic backbone curves are similar in shape, and these curves can all be divided into three stages: the initial linear elastic stage, the nonlinear phase near the peak point, and the descending stage after

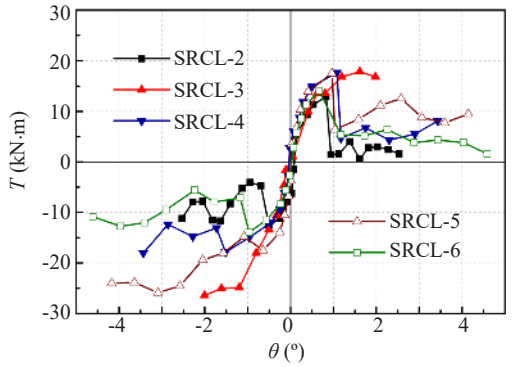

(a) Torsion-rotation angle backbone curves

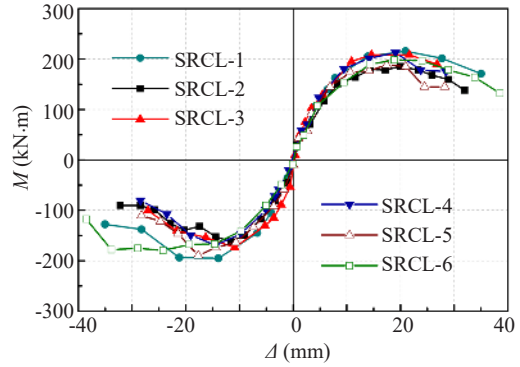

(b) Bending-displacement backbone curves

Fig. 11 Backbone curves

the peak point.

(2) At the beginning of loading, the slope of the backbone lines is closed, which reflects that the change of the γ and φ has little influence on the initial stiffness. However, after the load of the yield point, the backbone lines show different trajectories, and for the curves of backbone lines of the torsion moment versus rotation angle, these trajectories are quite different.

(3) The results corroborate the observations during the whole test. The specimen with large γ has a large limit torque, and if the γ of the specimens are the same, the specimen with large φ has a large limit torque.

4.3 Feature point parameter

Table 3 shows the feature point parameters such as crack point, yield point, peak point and the ultimate point of the specimen during the failure process. The yield point of the specimen in the table is calculated according to the energy equivalence method, and the ultimate points are equal to $0.85P_m$ (i.e., P_u=$0.85P_m$) at the descending segment of the skeleton curves. In Table 3, T represents the torsion load, P represents the bending load, Δ represents displacement, θ represents the twist angle, the subscript "y", "u", and "m" represent the yield point, peak point, and ultimate point, respectively,

Table 3 Characteristic parameters of specimens

No.	Loading direction	Yield point				Peak point				Ultimate point			
		T_y	θ_y	P_y	Δ_y	T_u	θ_u	P_u	Δ_u	T_m	θ_m	P_m	Δ_m
SRCL-1	+	—	—	194.68	11.72	—	—	223.46	21.06	—	—	189.94	31.86
	-	—	—	142.19	5.99	—	—	211.95	20.73	—	—	180.16	17.62
	Average	—	—	168.44	8.86	—	—	217.70	20.90	—	—	185.05	24.74
SRCL-2	+	11.30	0.55	172.01	10.38	12.70	0.81	188.44	18.91	10.80	0.87	160.17	27.46
	-	3.60	0.18	162.85	8.91	12.90	0.49	176.88	11.01	10.90	0.53	150.35	16.60
	Average	7.50	0.37	167.43	9.64	12.80	0.65	182.66	14.96	10.90	0.70	155.26	22.03
SRCL-3	+	15.30	0.98	214.56	14.55	17.70	1.61	218.39	15.31	15.10	1.87	185.63	29.55
	-	24.90	1.19	171.12	10.08	26.40	2.00	178.16	11.08	22.50	2.01	151.44	20.85
	Average	20.10	1.09	192.84	12.32	22.10	1.81	198.28	13.20	18.80	1.94	168.53	25.20
SRCL-4	+	13.90	0.58	215.49	12.89	17.70	1.08	215.52	12.89	15.10	1.12	183.19	24.82
	-	10.60	1.65	146.83	7.85	18.00	3.43	172.41	13.13	15.30	3.44	146.55	18.04
	Average	12.30	2.23	181.16	10.37	17.90	2.26	193.97	13.01	15.20	2.28	164.87	21.43
SRCL-5	+	15.60	0.54	147.18	6.35	17.30	0.95	192.53	15.73	14.70	1.01	163.65	21.64
	-	20.30	1.80	123.05	4.31	26.00	3.10	189.66	15.73	22.10	4.08	161.21	17.80
	Average	17.90	1.17	135.12	5.33	21.60	2.03	191.09	15.73	18.40	2.55	162.43	19.72
SRCL-6	+	11.00	0.47	201.51	13.33	14.10	0.67	218.21	18.95	12.00	0.71	185.48	30.65
	-	9.40	0.57	136.11	7.53	14.20	0.96	192.20	23.81	12.10	0.99	163.37	34.52
	Average	10.20	0.52	168.81	10.43	14.10	0.82	205.20	21.38	12.00	0.85	174.42	32.59

Note: The unit for the torsion load T in the table is (kN·m), the unit for the bending load P is (kN), the unit for the displacement Δ is (mm), the unit for the twist angle θ is (°).

"+" represents the push direction, and "-" represents the pull direction.

(1) The torsion load of the three specimens, SRCL-2 (γ=0.18), SRCL-4 (γ=0.25), and SRCL-5 (γ=0.29) are compared at the yield point, peak point, and ultimate point. It is easy to see that the torsion load at the yield point, peak point, and ultimate point becomes larger with the increase of γ; however, the bending load at this characteristic point increases first and then decreases.

(2) The torsion load of three specimens, SRCL-4 (φ=3.0), and SRCL-6 (φ=2.5) are compared at the yield point, peak point, and ultimate point. It is clear that the torsion load at the yield point, peak point, and ultimate point become smaller with the increase of φ, while the bending load at this characteristic point is greater.

(3) Note that the loading angle applied to the specimen SRCL-3 (γ=0.10, φ=3.0) was different from others, since the torsion load and bending load at characteristic points were even larger than that of RCL-5 (γ=0.29, φ=3.0).

4.4 Deformation capacity

The displacement ductility coefficient (μ_Δ) is calculated to evaluate accurate information of the ductility of the specimens, which is defined as the ratio of the ultimate displacement to the yield displacement ($\mu_\Delta=\Delta_m/\Delta_y$). The rotation angle ductility coefficient (μ_θ) is defined as the ratio of the angle corresponding to ultimate torsion to the rotation angle corresponding to yield torsion ($\mu_\theta=\theta_m/\theta_y$). The measured values of μ_Δ and μ_θ are given in Table 4. As shown in the table, the torsion ductility coefficient of the specimen is between 1.62 and 2.26, and the displacement ductility coefficient of the specimen is between 2.05 and 3.77. This indicated that the ductility is not adequate.

Figure 12 provides the comparison of rotation angle and displacement ductility coefficient of each specimen. Visible from the diagram, the displacement ductility coefficient is greater than the torsion ductility coefficient, for one specimen. It also reflects that, even with the presence of torsion, bending still governs the behavior of the failure mode of the specimen. Certainly, with the increasing of γ, the leading role of bending was weakened.

4.5 Interstory rotation angle

Table 5 shows the interstory rotation angle value corresponding to the deformation of each characteristic point of the specimen. The limit of the elastic interstory drift ratio and elastic-plastic interstory drift ratio for the CFST frame structure in design from the Chinese *Code for Seismic Design of Buildings* (GB 50011-2014) are 1/550 and 1/50, respectively.

As can be seen from Table 5, only the interstory drift ratio of specimen SRCL-3 at the cracking point and specimen SRCL-6 at the ultimate point reach the requirements of the *Code for Seismic Design of Buildings* (GB 50011-2014) of China, demonstrating that the interstory rotation angle deformation ability of the steel reinforced concrete L-shaped column is slightly weak.

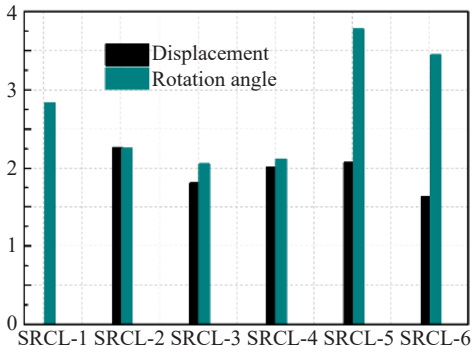

Fig. 12 Ductility coefficient comparisons of specimens

Table 4 Torsion ductility coefficient of specimens

Specimen No.	Direction	θ_y (mm)	θ_m (mm)	$\mu_\theta=\theta_m/\theta_y$	Average	Δ_y (mm)	Δ_m (mm)	$\mu_\Delta=\Delta_m/\Delta_y$	Average
SRCL-1	+	–	–	–	–	11.72	31.86	2.72	2.83
	-	–	–	–		5.99	17.62	2.94	
SRCL-2	+	0.55	0.87	1.58	2.26	10.38	27.46	2.65	2.25
	-	0.18	0.53	2.94		8.91	16.60	1.86	
SRCL-3	+	0.98	1.87	1.91	1.80	14.55	29.55	2.03	2.05
	-	1.19	2.01	1.69		10.08	20.85	2.07	
SRCL-4	+	0.58	1.12	1.93	2.01	12.89	24.82	1.93	2.11
	-	1.65	3.44	2.08		7.85	18.04	2.30	
SRCL-5	+	0.54	1.01	1.87	2.07	6.35	21.64	3.41	3.77
	-	1.80	4.08	2.27		4.31	17.80	4.13	
SRCL-6	+	0.47	0.71	1.51	1.62	13.33	30.65	2.30	3.44
	-	0.57	0.99	1.74		7.53	34.52	4.59	

The relevant restrictions in international codes are summarized in Table 6. According to the characteristics of specimens and the literature reported by Li (2011), in the *International Building Code* 2009 (IBC-2009), displacement limitation conditions is other structure of importance II; in *Design of Structures for Earthquake Resistance* 2004 (EC8-2004), displacement limitation conditions is structure of importance II combined with a non-ductility component. Residential height is 3600 mm. The interstory rotation angle is limited in *Building Standard Law* 1981 (BSL-1981) and *Code for Seismic Design of Buildings* (GB50011-2014). Typically, 1/200 and 1/100 are the first level design requirements and the second level design requirements, respectively, in *Building Standard Law* 1981 (BSL-1981).

It is seen from Table 6 that the yield point displacement of the specimens can meet the requirements of American and European codes, but the failure point displacement can only meet the requirements of the American codes. The interstory rotation angle of the specimen cannot meet the requirements of the Japanese code at the crack point. However, SRCL-6 specimens can meet the second level design requirements of the Japanese code.

Table 5 Interstory rotation angle of specimens

Specimen No.	Direction	Crack	Yield	Peak	Ultimate
SRCL-1	+		1/107	1/56	1/42
	-	1/4720	1/127	1/84	1/56
	Average	1/6940	1/116	1/67	1/48
SRCL-2	+	1/1340	1/110	1/58	1/40
	-	1/682	1/160	1/100	1/64
	Average	1/900	1/130	1/74	1/50
SRCL-3	+	1/340	1/120	1/54	1/44
	-	1/463	1/163	1/109	1/63
	Average	1/390	1/139	1/73	1/52
SRCL-4	+	1/1009	1/115	1/62	1/50
	-	1/830	1/120	1/82	1/60
	Average	1/908	1/117	1/70	1/55
SRCL-5	+	1/534	1/122	1/67	1/50
	-	1/1124	1/110	1/67	1/60
	Average	1/738	1/115	1/67	1/55
SRCL-6	+	1/690	1/85	1/50	1/30
	-	1/715	1/77	1/40	1/27
	Average	1/700	1/80	1/45	1/29

4.6 Energy dissipation capacity

The equivalent damping coefficient (h_e) is used to characterize the energy dissipation of specimens in seismic analysis, which can be calculated as Eq. (7):

$$h_e = \frac{S_{(ABC + CDA)}}{2\pi S_{(OBF + ODE)}} \tag{7}$$

where $S_{(ABC+CDA)}$ is the area surrounded by a cyclic hysteresis loop and $S_{(OBF+ODE)}$ refers to the sum area of the triangle *OBF* and *ODE* as shown in Fig. 13. The curve is the first hysteretic loop in displacement amplitude during the displacement-controlled phase. Values of the equivalent damping ratio (h_e) on various displacement levels nΔ_y are shown in Table 7 and Figs. 14 and 15. *M* represents the bending energy dissipation, *T* represents the torsion energy dissipation, and *M*+*T* represents the bending and torsion energy dissipation.

(1) With the increase of displacement, the torsion energy dissipation of the specimen shows the trend of slow decline, and the energy dissipation value is between 0.024 and 0.463. The bending energy dissipation curve of each specimen increases in a fan-shaped way, and the energy dissipation value is between 0.087 and 0.282. The total energy consumption of both remained stable and slightly increased in the later stage, and the total energy consumption value ranged from 0.087 to 0.548.

(2) At the time of failure, the damping ratio of the specimen with γ=0 is the smallest, and ranged from 0.087 to 0.169. However, the damping ratio of the specimen with γ=0.10 to 0.29 is larger, between 0.102 and 0.548, which reflects the effect of torsion, and causes the specimen to consume more energy and results in more serious damage to the material.

Figure 15 shows the composition of the total energy consumption and the trend of the proportion of bending and torsion. As shown in Fig. 15 (a), before loading to 5Δy, the total energy dissipation of the specimen remains stable, and it begins to obviously increase

Table 6 International code requirements

	USA	Europe	Japan	China
Name of code	International Building Code 2009 (IBC-2009)	Design of Structures for Earthquake Resistance 2004 (EC8-2004)	Building Standard Law 1981 (BSL-1981)	Code for Seismic Design of Buildings (GB 50011-2014)
Displacement/mm	72	13.5	-	-
interstory rotation angle	-	-	1/200 1/100	1/550

after $6\Delta_y$. As shown in Fig. 15 (b), in the early stage of energy dissipation, torsion energy dissipation is the main component, accounts for 70% of the total energy consumption, and decreases gradually as the deformation increases. During $1\Delta_y$ to $3\Delta_y$, it decreases slowly, while it accelerates during $3\Delta_y$ to $5\Delta_y$, and falls below 50% when at $5\Delta_y$. After that, the energy dissipation of the specimen is dominated by bending energy dissipation. At the $7\Delta_y$, torsion energy dissipation and bending energy dissipation, the discrete trend is dramatically enlarged. In the total energy consumption, the proportion of bending energy consumption has increased to 60%, which determines the final failure process of the specimen.

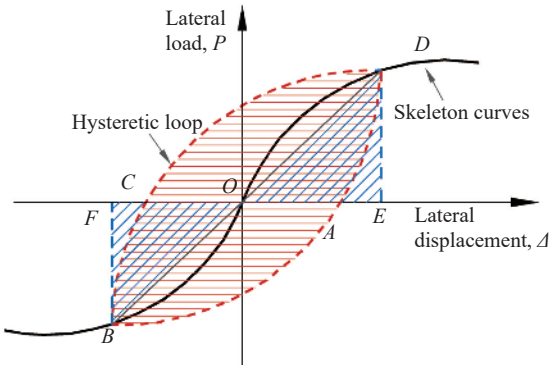

Fig. 13 Calculation diagram of equivalent damping ratio

4.7 Stiffness degradation

Based on the change of secant stiffness of rotation angles and lateral displacements backbone curve, the

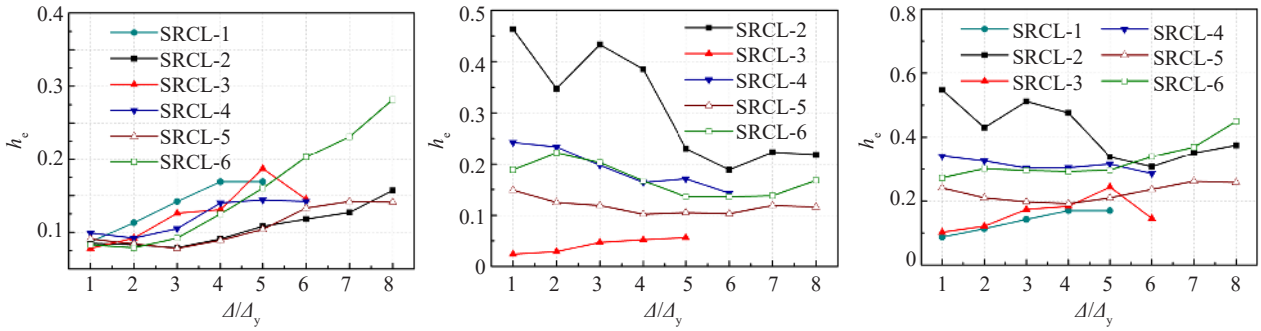

(a) h_e of bending (b) h_e of torsion (c) h_e of bending and torsion

Fig. 14 Damping coefficients of specimens

Table 7 Equivalent damping ratio of specimens

Specimen No.	Energy dissipation	$1\Delta_y$	$2\Delta_y$	$3\Delta_y$	$4\Delta_y$	$5\Delta_y$	$6\Delta_y$	$7\Delta_y$	$8\Delta_y$
SRCL-1	*M*	0.087	0.113	0.142	0.169	0.169			
	T	—	—	—	—	—			
	M+*T*	0.087	0.113	0.142	0.169	0.169			
SRCL-2	*M*	0.085	0.083	0.079	0.091	0.108	0.118	0.127	0.157
	T	0.463	0.347	0.433	0.385	0.230	0.189	0.223	0.218
	M+*T*	0.548	0.430	0.512	0.476	0.338	0.307	0.350	0.375
SRCL-3	*M*	0.078	0.092	0.126	0.131	0.187	0.145		
	T	0.024	0.029	0.047	0.052	0.056			
	M+*T*	0.102	0.121	0.173	0.183	0.243	0.145		
SRCL-4	*M*	0.099	0.092	0.105	0.140	0.144	0.142		
	T	0.242	0.233	0.198	0.164	0.171	0.143		
	M+*T*	0.341	0.325	0.303	0.304	0.315	0.285		
SRCL-5	*M*	0.091	0.084	0.078	0.089	0.104	0.133	0.142	0.141
	T	0.149	0.125	0.119	0.102	0.105	0.103	0.119	0.116
	M+*T*	0.240	0.209	0.197	0.191	0.209	0.236	0.261	0.257
SRCL-6	*M*	0.083	0.079	0.092	0.125	0.160	0.203	0.231	0.282
	T	0.189	0.222	0.203	0.167	0.136	0.136	0.138	0.168
	M+*T*	0.272	0.301	0.295	0.292	0.296	0.339	0.369	0.450

torsion and bending stiffness degradation processes of the specimens are investigated. According to Eq. (8):

$$K_{\Delta}=\frac{|+P_i|+|-P_i|}{|+\Delta_i|+|-\Delta_i|},\ K_{\theta}=\frac{|+T_i|+|-T_i|}{|+\theta_i|+|-\theta_i|} \tag{8}$$

where K_{Δ} and K_{θ} are bending stiffness and torsion stiffness corresponding to the peak points of hysteretic respectively; P_i and T_i are peak shear and peak torsion during the first cycle of $n\Delta_y$ (n = 1, 2, 3…) lateral displacement, respectively; Δ_i and θ_i are displacements and rotation angles corresponding to the peak shear and peak torsion, respectively; and "+" and "-" are positive and reverse loading directions, respectively. To better observe the trend of stiffness degeneration, the normalization torsion stiffness and bending stiffness degradation curves are given in Fig. 16.

As shown in the figure, when compared with bending stiffness, the early degradation of torsional stiffness is more serious. At $2\theta_y$, the degradation of torsion stiffness is basically over 80%, while the bending stiffness degradation is only 50%–60%. In the later stage, both slow down, however, their residual stiffness is very small, only about 20%.

It also can be seen from Fig. 16 (a), except for specimen SRCL-3 (γ=0.10, φ=3.0) that had a different loading angle applied, the trend of the other four specimen's torsion stiffness degradation curves are similar, indicating that the change of γ (compared the specimen SRCL-2, SRCL-4, and SRCL-5) and φ (compared the specimen SRCL-4 and SRCL-6) has no significant effect on torsion stiffness degradation. The same rule in bending stiffness degradation is observed from Fig. 16(b).

5 Conclusions

(1) According to the variation of γ, the failure modes of the SRC L-shaped columns subjected to combined constant axial compression and cyclic reverse bending-shear-torsion loading can be divided into three types: bending, bending-shear, and bending-torsion failure. They are manifested as concrete crushing and falling, and the spiral diagonal cracks are wider in width and larger in number in the specimen with larger γ.

(2) The torsion-twist angle and bending-displacement hysteresis curves presented asymmetric reverse S-shaped pinching the middle. After the peak point, the rotation angle hysteresis curve has an obvious "load drop" phenomenon.

(3) The specimen with a large γ has a large corresponding torsion at the yield point. If the specimens have the same γ and different φ, the one with the larger φ has greater corresponding torsion and bending at yield, peak value, and failure point.

(4) In this study, the ultimate interstory drift ratio of the damage point of the specimen is generally less than that of the Chinese *Code for Seismic Design of Buildings* (GB 50011-2014), which is insufficient.

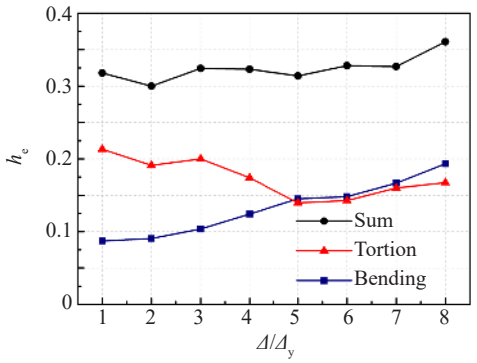

(a) The trend of the proportion of h_e

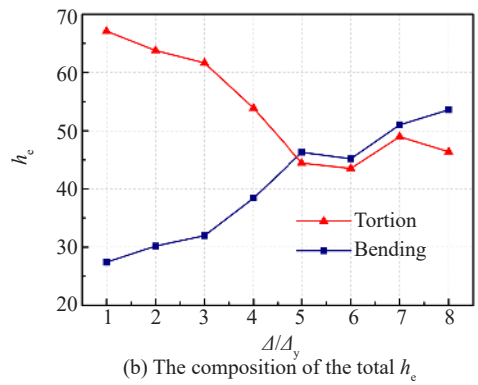

(b) The composition of the total h_e

Fig. 15 Component of damping coefficients of specimens

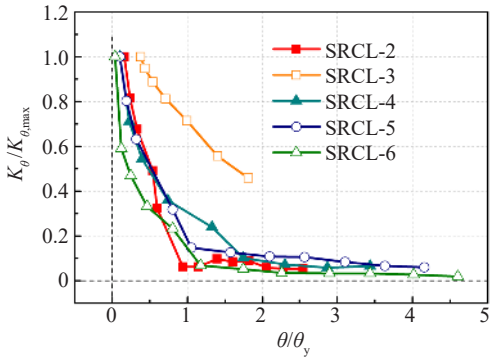

(a) Torsion stiffness degradation curves

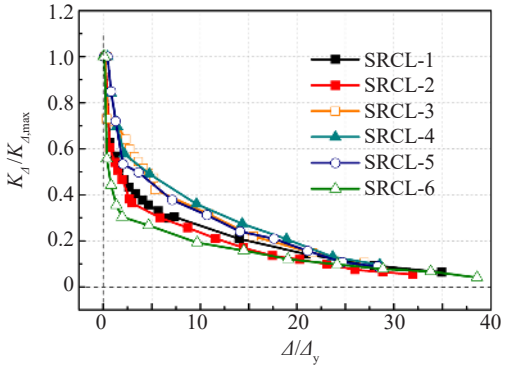

(b) Bending stiffness degradation curves

Fig. 16 Stiffness degradation curves

(5) The equivalent damping coefficient of the failure point of the specimen is between 0.169 and 0.450 (the torsion and bending energy dissipation of final displacement amplitude during displacement-controlled phase), the energy consumption in the prophase is mainly caused by torsion while the anaphase is by bending. It can be concluded that the failure of the specimen is ultimately governed by the bending moment, from the analysis of rotation angle, displacement ductility coefficient, and the failure process of the specimen.

(6) The torsion stiffness degradation is more serious than those of bending, with a great difference in early degradation.

Acknowledgement

The research reported herein was supported by the National Natural Science Foundation of China (Nos. 51268004 and 51578163), Natural Science Foundation of Guangxi (project No. 2016GXNSFDA380032) and Bagui Scholar Program of Guangxi (No. [2019]79). This financial support is gratefully acknowledged.

References

Arnold C (1980), "Building Configuration: Characteristics for Seismic Design," *Proceedings of the Seventh World Conference on Earthquake Engineering*, **4**: 589–592.

Arabzadeh H and Galal K (2018), "Seismic-Response Analysis of RC C-Shaped Core Walls Subjected to Combined Flexure, Shear, and Torsion," *Journal of Structural Engineering*, **144**(10).

Chen ZP, Xu JJ and Chen YL (2016), "Axial Compression Ratio Limit Values for Steel Reinforced Concrete (SRC) Special Shaped Columns," *Steel & Composite Structures*, **20**(2): 295–316.

Chen ZP, Xu JJ and Xue JY (2015), "Hysteretic Behavior of Special Shaped Columns Composed of Steel and Reinforced Concrete (SRC)," *Earthquake Engineering and Engineering Vibration*, **14**(2): 329–345.

Chen ZP and Liu X (2018), "Seismic Behavior of Steel Reinforced Concrete Cross-Shaped Column Under Combined Torsion," *Steel and Composite Structures*, **16**(4): 407–420.

Chen SC, Peng W, Yan WM (2018), "Experimental Study on Steel Reinforced Concrete Columns Subjected to Combined Bending-Torsion Cyclic Loading," *Structural Design of Tall and Special Buildings*, **27**(11).

Duan XN and Chandler AM (2010), "Seismic Torsional Response and Design Procedures for a Class of Setback Frame Buildings," *Earthquake Engineering & Structural Dynamics*, **24**(5): 761–777.

ECN. Eurocode 8 (2004), *Design of Structures for Earthquake Resistance — Part 1-General Rules, Seismic Actions and Rules for Buildings*, European Committee for Standardization, Bruxelles, Belgium.

Fang L, Zhang B and Jin GF (2015), "Seismic Behavior of Concrete-Encased Steel Cross-Shaped Columns," *Journal of Constructional Steel Research*, **109**: 24–33.

Greene G and Belarbi A (2009), "Model for Reinforced Concrete Members under Torsion, Bending, and Shear. I: Theory," *Journal of Engineering Mechanics*, **135**(9): 970–977.

GB/T 50081-2002 (2002), *Standard for Test Method of Mechanical Properties on Ordinary Concrete*, China Building Industry Press, Beijing, China. (in Chinese)

GB/T228.1 (2010), *Metallic Materials-Tensile Testing-Part 1 Method of Test at Room Temperature*, China Standards Press, Beijing, China. (in Chinese)

GB50011-2014 (2014), *Code for Seismic Design of Buildings*, China Building Industry Press, Beijing, China. (in Chinese)

Hsu HL and Wang C (2000), "Flexural–Torsional Behaviour of Steel Reinforced Concrete Members Subjected to Repeated Loading," *Earthquake Engineering & Structural Dynamics*, **29**(5): 667–682.

Hsu HL, Hsieh JC and Juang J (2004), "Seismic Performance of Steel-Encased Composite Members with Strengthening Cross-Inclined Bars," *Journal of Constructional Steel Research*, **60**(3): 1663–1679.

IBC (2009), *International Building Code*, International Code Council, Inc, 12009.

Ji XD, Liu D, and Qian JR (2017), "Improved Design of Special Boundary Elements for T-Shaped Reinforced Concrete Walls," *Earthquake Engineering and Engineering Vibration*, **16**(1): 83–95.

Jurkowska N (2018), "Considering Nonlinear Properties of Concrete in the Design of Reinforced Concrete Structures for Torsion," *Materials Science and Engineering*, **364**(1): 1–9.

Kaushik S and Dasgupta K (2019), "Seismic Behavior of Slab-Structural Wall Junction of RC Building." *Earthquake Engineering and Engineering Vibration*, **18**(2): 331–349.

Koliopulos PK, Hsieh JC and Chandler AM (1995), "Stochastic Linearization of Inelastic Seismic Torsional Response: Formulation and Case Studies", *Engineering Structures*, **17**(7): 494–504.

Li B and Pham TP (2014), "Experimental Study on the Seismic Response of L-Shaped Reinforced Concrete Columns," *Structures Congress 2014*, 1673–1682.

Li H (2011), "The Seismic Action Comparison Between Chinese, American, European and Japanese Seismic Design Codes for Buildings," *Master Dissertation*, Harbin Institute of Technology, Harbin, China. (in Chinese)

Li Q and Belarbi A (2012), "Performance Based Design Approach for RC Square Bridge Columns under

Combined Loadings Including Torsion," *Structure Congress*, **2012**: 2223–2234.

Li Q and Belarbi A (2013), "Damage Assessment of Square RC Bridge Columns Subjected to Torsion Combined with Axial Compression, Flexure, and Shear," *KSCE Journal of Civil Engineering*, **17**(3): 530–539.

Marin J (1979), "Design Aids for L-Shaped Reinforced Concrete Columns," *ACI Structural Journal*, **76**(11): 1197–1216.

Li Z, Qin H and Dang H (2008), "Experimental Study on Mechanical Property of Steel Reinforced Concrete L-Shaped Short Columns," *International Journal of Modern Physics B*, **22**(31n32): 5755–5761.

Liang QQ, Uy B and Liew JYR (2008), "Local Buckling of Steel Plates in Concrete-Filled Thin-Walled Steel Tubular Beam-Columns," *Steel Construction*, **63**(3): 396–405.

Liu ZQ, Li K and Xue JJ *et al*. (2018), "Seismic Damage Experiment and Numerical Simulation of Steel Reinforced Concrete T-Shaped Column," *Earthquake Engineering and Engineering Dynamics*, **38**(5): 85–92. (in Chinese)

Liu ZQ, Li K and Xue JJ *et al*. (2019), "Experimental Study and Finite Element Analysis on Seismic Behavior of Solid-Web Steel Reinforced Concrete Cross-Shaped and L-Shaped Columns," *Journal of Building Structures*, **40**(4): 104–115. (in Chinese)

Liu ZQ, Xue JY and Zhao HT (2016), "Seismic Behavior of Steel Reinforced Concrete Special-Shaped Column-Beam Joints," *Earthquakes & Structures*, **11**(4): 65–680.

Nie JG, Wang YH and Fan JS (2012), "Experimental Study on Seismic Behavior of Concrete Filled Steel Tube Columns Under Pure Torsion and Compression–Torsion Cyclic Load," *Journal of Constructional Steel Research*, **79**(1): 115–126.

Nie JG, Wang YH and Fan JS (2013), "Experimental Research on Concrete Filled Steel Tube Columns Under Combined Compression-Bending-Torsion Cyclic Load," *Thin-Walled Structures*, **67**(2): 1–14.

Otuka H, Takeshita E and Urakawa Y (2005), "Seismic Performance and Correlation Characteristics of Reinforced Concrete Columns Subjected to Torsional Moment, Bending Moment/Shear Force and Axial Force," *Doboku Gakkai Ronbunshu*, **81**: 123–139.

Patton ML and Singh KD (2012), "Numerical Modeling of Lean Duplex Stainless Steel Hollow Columns of Square, L-, T-, And +-Shaped Cross Sections Under Pure Axial Compression," *Thin-Walled Structures*, **53**: 1–8.

Patton ML and Singh KD (2014), "Finite Element Modelling of Concrete-Filled Lean Duplex Stainless Steel Tubular Stub Columns," *International Journal of Steel Structures*, **14**(3): 619–632.

Prakash S, Belarbi A and You YM (2010), "Seismic Performance of Circular RC Columns Subjected to Axial Force, Bending, and Torsion with Low and Moderate Shear," *Steel Construction*, **32**(1): 46–59.

Ramamurthy LN and Khan TAH (1986), "Closure of L-Shaped Column Design for Biaxial Eccentricity," *Journal of Structural Engineering*, **112**(10): 2360–2362.

Rong B, Feng CX, Zhang RY, *et al*. (2017), "Compression-bending Performance of L-shaped Column Composed of Concrete Filled Square Steel Tubes under Eccentric Compression," *International Journal of Steel Structures*, **17**: 325–337.

Rong X, Qiao CN and Yang CH (2018), "Seismic Behavior Test and Finite Element Analysis of Steel Reinforced Concrete Cross-Shaped Columns," *Earthquake Engineering and Engineering Dynamics*, **38**(2): 63–71. (in Chinese)

Shen ZY, Lei M and Li YQ (2013), "Experimental Study on Seismic Behavior of Concrete-Filled L-Shaped Steel Tube Columns," *Advances in Structural Engineering*, **16**(7): 1235–1248.

Sun R, Burgess IW and Huang Z (2015), "Progressive Failure Modelling and Ductility Demand of Steel Beam-to-Column Connections in Fire," *Engineering Structures*, **89**(17): 66–78**.**

Tirasit P and Kawashima K (2007), "Seismic Performance of Square Reinforced Concrete Columns under Combined Cyclic Flexural and Torsional Loadings," *Journal of Earthquake Engineering*.

Teixeira MM and Bernardo LFA (2018), "Ductility of RC Beams Under Torsion," *Engineering Structures*, **168**: 759–769.

Wang P, Han Q and Du XL (2014), "Seismic Performance of Circular RC Bridge Columns with Flexure–Torsion Interaction," *Soil Dynamics & Earthquake Engineering*, **66**(66): 13–30.

Wang YH, Wang W and Chen J (2018), "Seismic Behavior of Steel Tube Confined RC Columns Under Compression-Bending-Torsion Combined Load," *Journal of Constructional Steel Research*, **143**: 83–96.

Weng XH, Shao YJ and Lao YH *et al*., (2017), "Experimental Study on Seismic Behavior of Steel Reinforced Concrete Column Under Combined Torsion," *Journal of Building Structure*, **38**(11): 23–33.

Xiao CZ, Deng F and Chen T *et al*. (2017), "Experimental Study on Concrete-Encased Composite Columns with Separate Steel Sections," *Steel & Composite Structures*, **23**(4): 483–491.

Xiang P, Deng ZH and Su YS (2017), "Experimental Investigation on Joints Between Steel-Reinforced Concrete T-Shaped Column and Reinforced Concrete Beam Under Bidirectional Low-Cyclic Reversed Loading," *Advances in Structural Engineering*, **20**(3): 446–460.

Xue JY, Chen ZP and Zhao HT (2012), "Shear Mechanism and Bearing Capacity Calculation on Steel Reinforced Concrete Special-Shaped Columns," *Steel & Composite Structures*, **13**(5): 473–487.

Xue JY, Zhou CF and Liu ZQ (2017), "Research on Damage of Solid-Web Steel Reinforced Concrete T-Shaped Columns Subjected to Various Loadings," *Steel and Composite Structures*, **25**(5): 603–615.

Yang Y, Yang H and Zhang S (2010), "Compressive Behavior of T-Shaped Concrete Filled Steel Tubular Columns," *International Journal of Steel Structures*, **10**(4): 419–430.

Yuan SQ, Chen SC, Tian Y, *et al*. (2018), "Experimental Study and Analysis of Torsion-Bending Ratio Effect on Aseismic Performance of SRC Columns," *Engineering Mechanics*, **35**(03): 167–177.

Zhang AL, Yu J and Xu M (2010), "Experiment Research on Steel Specially Columns with Cruciform Section Under Loading," *Journal of Building Structures,* **31**(2): 11–19.

Zuo ZL, Cai J and Yang C (2012), "Axial Load Behavior of L-Shaped CFT Stub Columns with Binding Bars," *Engineering Structures*, **37**: 88–98.

Zhou T, Chen Z and Liu H (2012), "Seismic Behavior of Special Shaped Column Composed of Concrete Filled Steel Tubes," *Journal of Constructional Steel Research*, **75**(75): 131–141.